

Hard X-ray photoelectron spectroscopy reveals self-organized structures of electrocatalytic nickel oxy-hydroxides

Filippo Longo^{a,c}, Emanuel Billeter^{a,c}, Selim Kazaz^{a,c}, Alessia Cesarini^{b,c}, Marin Nikolic^{a,c}, Aarati Chacko^{d,e}, Patrik Schmutz^f, Zbynek Novotny^{g,f}, Andreas Borgschulte^{a,c,*}

^a Department of Chemistry, University of Zürich, Winterthurerstrasse 190, 8057 Zürich, Switzerland

^b Institute for Chemical and Bioengineering, Department of Chemistry and Applied Biosciences, ETHZ, 8093 Zürich, Switzerland

^c Laboratory for Advanced Analytical Technologies, Empa - Swiss Federal Laboratories for Materials Science and Technology, Überlandstrasse 129, 8600 Dübendorf, Switzerland

^d Nanosciences, Faculty of Science, University of Basel, Klingenbergstrasse 82, 4056 Basel, Switzerland

^e Laboratory for Magnetic and Functional Thin Films, Empa - Swiss Federal Laboratories for Materials Science and Technology, Überlandstrasse 129, 8600 Dübendorf, Switzerland

^f Laboratory for Joining Technologies & Corrosion, Empa - Swiss Federal Laboratories for Materials Science and Technology, Überlandstrasse 129, 8600, Dübendorf, Switzerland

^g Swiss Light Source, Paul Scherrer Institut, CH-5232, Villigen-PSI, Switzerland

ARTICLE INFO

Keywords:

Alkaline electrolysis
Nickel oxy-hydroxide
Hard X-ray photoelectron spectroscopy
Near ambient-pressure photoelectron spectroscopy
electrochemical impedance

ABSTRACT

Alkaline water electrolysis represents one of the simplest methods employed for renewable hydrogen production, reaching high conversion efficiency utilizing cheap and abundant transition metals such as nickel and its alloys. The outstanding properties of Ni-materials do not arise from the metallic host, rather from the surface passivated with various oxidized compounds formed during the electrochemical process. This newly formed layer is responsible for the catalytic properties of the system, therefore the investigation of its evolution as function of potential and time is crucial for a deeper understanding of the overall electrochemical process. However, the characterization of the chemical environment at the topmost layer, as well as the underlying layers, is complex and requires surface sensitive techniques. Here, we show that while ambient pressure soft X-ray photoelectron spectroscopy (APXPS) allows to follow the changes of the topmost layer, characterization of the deeper layers modifications occurring during electrocatalysis requires a combination of soft- and hard X-ray photoelectron spectroscopy (XPS/HAXPES), coupled with electrochemical impedance spectroscopy (EIS). The findings show how the high electrocatalytic activity of Ni (oxy)-hydroxides is directly related to the increasing water intercalation into the passivation layer, which supports the long-debated hypothesis of a water mediated OH⁻ diffusion mechanism. High performance of the electrode is promoted by the peculiar structure of the surface, which self-organizes during the initial formation of the passivation layer enabling self-healing during electro-catalysis. Ultimately, we show how the investigation at different depths by means of XPS/HAXPES in combination with EIS allows a better understanding of the chemical changes occurring throughout the passivation layer, signaling a paradigm shift from the traditional explanation of electro-catalysis by a simple electrode material with a stable nanostructure, to a concept leaning towards a dynamic electrochemical interface.

1. Introduction

Water electrolysis is an electrochemical process based on the oxidation/reduction of water at electrode/electrolyte interface without detrimental modification of the electrodes [1]. The latter aspect distinguishes this process from many other electrochemical reactions and translates into a defiant prerequisite of the electrode material: the

materials have to be stable under harsh chemical environments (very high/low pH/potential applied), while being electro-catalytically active [2]. The stability of materials in electrochemical environments has been categorized in Pourbaix diagrams [3]. The Pourbaix's famous atlas [3] showcases that only very few materials are stable under the required conditions, particularly in acidic media. Nevertheless,

* Corresponding author at: Laboratory for Advanced Analytical Technologies, Empa - Swiss Federal Laboratories for Materials Science and Technology, Überlandstrasse 129, 8600 Dübendorf, Switzerland.

E-mail addresses: filippo.longo@empa.ch (F. Longo), andreas.borgschulte@empa.ch (A. Borgschulte).

<https://doi.org/10.1016/j.susc.2023.122397>

Received 9 March 2023; Received in revised form 25 August 2023; Accepted 24 September 2023

Available online 30 September 2023

0039-6028/© 2023 The Author(s). Published by Elsevier B.V. This is an open access article under the CC BY license (<http://creativecommons.org/licenses/by/4.0/>).

there are non stable materials that can form passivation layers, which eventually stabilize them. Nickel, as an archetypal representative of this materials class, is still one of the best electrode materials for alkaline water electrolysis [2,4–6], due to its relative abundance, low-cost, stability, and durability, while being electro-catalytically active. However, the newly formed electro-catalytically active layers, with its properties dependent on applied conditions, complicate the rational development and the improvement of electrodes such as Ni-Fe [7–12], because the structure and thus performance is determined in retrospect. Furthermore, identification of the electrochemically active sites is complicated by the transient (oxy)-hydroxide layers exhibiting various Ni species as well as counter ions, with their existence and amount dependent on the applied conditions [13–15]. Although only the topmost layer is in general responsible for the electro-catalytic process [16], its properties depend on the underlying ones [17]. This fact is often neglected because the characterization of such an extended surface of several nm thickness is challenging. Medway et al. probed the peculiar passivation layer structure upon electrochemical treatment of Ni-electrodes using grazing incidence X-ray scattering [4]. However, the method relies on a variety of assumptions, in particular that the layers are uniform. Among the various surface sensitive techniques, X-ray photoelectron spectroscopy (XPS) turns out to be one of the most surface sensitive, also giving information on the chemical environment of the elements present in the sample [18,19]. While XPS is perfectly suited for the investigation of the outermost layers, it lacks information on the deeper layers. Hard X-ray photoelectron spectroscopy (HAXPES) can provide the sought information due on the longer mean free path length of high-energy electrons of up to 20–30 nm [20]. The combination of both techniques HAXPES and XPS is a powerful tool to correlate surface and bulk chemistry [21].

In this paper, we combine various X-ray photoelectron spectroscopy techniques for the preparation and monitoring of oxide/hydroxide layer formation as a function of potential and time together with electrochemical impedance spectroscopy (EIS) serving as a blue print for the characterization of electrocatalytically active metals forming passivation layers (Fig. 1). This includes the formation of the initial oxide/hydroxide layer on the clean metal layer; an often neglected, but unavoidable step in the preparation procedure. Subsequently, we follow the evolution of the chemical and electronic structure upon applying a potential with particular focus on the extended surface, i.e., the layers below the topmost surface layer that are not accessible to XPS but are accessible to HAXPES. These layers are found to consist of Ni (oxy)-hydroxides self-organizing on the nickel electrode in a functional way beneficial for electrocatalysis.

2. Methods

2.1. Nickel etching procedure

Ni foil was purchased from Goodfellow (99.98% purity, 25 × 25 mm, 0.05 mm thickness) and used as WE after surface treatment. The chemical etching of Ni foil was performed inside the glovebox as follows [22]: the electrode was dipped in a solution prepared with 30 mL of HNO₃, 10 mL of H₂SO₄, 10 mL of H₃PO₄, and 50 mL of glacial CH₃COOH for 2 min at room temperature and thoroughly rinsed with Milli-Q water. Milli-Q water as well as the purified KOH used for the electrochemical process were degassed for 30 min with Ar inside the glovebox.

2.2. Purification of KOH electrolytic solution

Electrochemical characterization was performed in 1 M Fe-free KOH electrolytic solution. The solution was prepared following a procedure present in literature [7]. In a H₂SO₄-cleaned 50 mL polypropylene centrifuge tube, ~2 g of 99.999% Ni(NO₃)₂·6 H₂O were dissolved in ~4 mL of 18.2 MΩ cm H₂O. 20 mL of 1 M KOH were added to precipitate high-purity Ni(OH)₂. The mixture was shaken and centrifuged, and the

supernatant was decanted. The Ni(OH)₂ then underwent three washing cycles by adding ~20 mL of 18.2 MΩ cm water and ~2 mL of 1 M KOH to the tube, redispersing the solid, centrifuging, and decanting the supernatant. Finally, the tube was filled with 50 mL of 1 M KOH for purification. The solid was redispersed and mechanically agitated for at least 10 min, followed by at least 3 h of resting. The mixture was centrifuged, and the purified KOH supernatant was decanted into a H₂SO₄-cleaned polypropylene bottle for storage.

2.3. Electrochemical characterization

A Hg/HgO electrode filled with 0.1 M KOH as internal electrolyte solution was used as reference electrode (RE) ($E_0 \sim -70$ mV vs. SCE). A Pt wire (99.99% purity) was used as counter electrode (CE). The cyclic voltammogram and impedance spectra were recorded in 1 M Fe-free KOH solution, using a Metrohm Autolab PGSTAT204 with additional FRA32M module for EIS and NOVA 2.1.5 for the data evaluation. The cyclovoltammogram of the sample (Fig. 2) was recorded at the end of the experiment at a scan rate of 0.1 V/s from +0.7 V to −1.3 V vs. RE. Impedance spectra were recorded with an AC amplitude of 10 mV rms by sweeping the frequency from 10⁵ Hz to 0.1 Hz at 10 points per decade. All the data were recorded in a single sine mode. The electrochemical analysis was performed in a tailored glove-box connected to the introduction chamber of the X-ray spectrometer with a continuous flow of argon gas. The chamber was flushed with argon; experiments were started when reaching a relative humidity value below 10%. Schematic of the experiment (Fig. S1 in Supporting Information) describes the three different phases of the experimental procedure. The pre-treatment phase consisted of an etching step of the Ni foil (performed as described in Section 2.1) and a dipping step in alkaline solution at open circuit potential (OCP) for 10 s, with the latter performed after thoroughly rinsing with Milli-Q water. The etching step was performed in order to restore the metallic surface by removing the native oxide/hydroxide layer developed on the surface during unavoidable exposure to moist air [4,23,24]. The dipping step was performed to obtain a first reference system for the evaluation of the passivation layer, as it is the starting surface subsequently modified electrochemically. This surface can be compared to the one prepared under better defined conditions (see Section 2.5). The sample resulting from the combination of these preliminary steps has been referred to as Ni1. During the application of potential, current was recorded with a step of 10 ms. Afterwards, the nickel electrode was tested under anodic (+0.6 V vs. RE) and cathodic (−1.2 V vs. RE) conditions for different times (see Table T1 in Supporting Information), in order to obtain informations about passivation layer modifications during oxygen evolution reaction (OER) and hydrogen evolution reaction (HER) (Fig. 2). The impedance measurements were performed after the application of OCP (see Table T14 in Supporting Information) in order to minimize any process occurring at the interface. Before starting a new cycle, a small portion of the electrode was cut for the post-mortem XPS/HAXPES analysis. Sample obtained under anodic conditions has been referred to as Ni2, 3, 4 and 5 while samples obtained under cathodic conditions as Ni6, 7 and 8. In this paper, we study the formation of Ni oxy-hydroxides by photoemission and impedance spectroscopy. Various allotropes are known [13,14,25]. As photoemission spectroscopy is not very sensitive to the crystal structure, we cannot distinguish the allotropes. Anyway, XPS detects a high amount of water, pointing towards the presence of α -Ni(OH)₂ and γ -NiOOH in the sample as the phases with high amount of crystal water [13].

2.4. Surface characterization

The post-mortem XPS/HAXPES analysis was performed using a PHI Quantes spectrometer (ULVAC-PHI), equipped with a conventional low-energy Al-K α source (1486.6 eV) and a high energy Cr-K α (5414.7 eV)

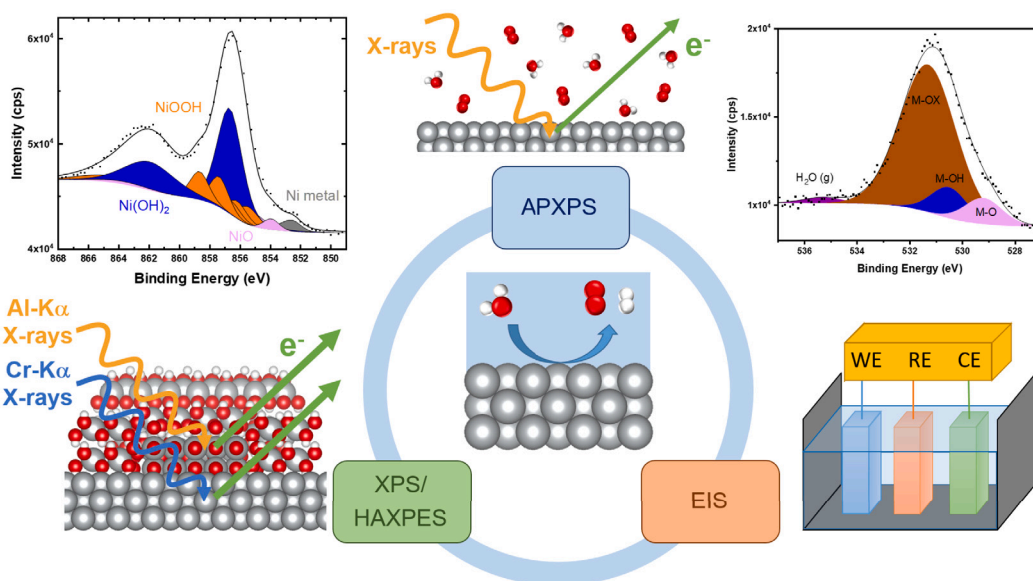


Fig. 1. Concept of the experiment. Schematic representation of the techniques used in this work to investigate the oxidation of clean nickel surface upon exposure to O_2 and/or H_2O (APXPS, blue), the electrochemical evolution of the system over time in different conditions (EIS, orange) and the surface/bulk modifications after alkaline water splitting (XPS/HAXPES, green).

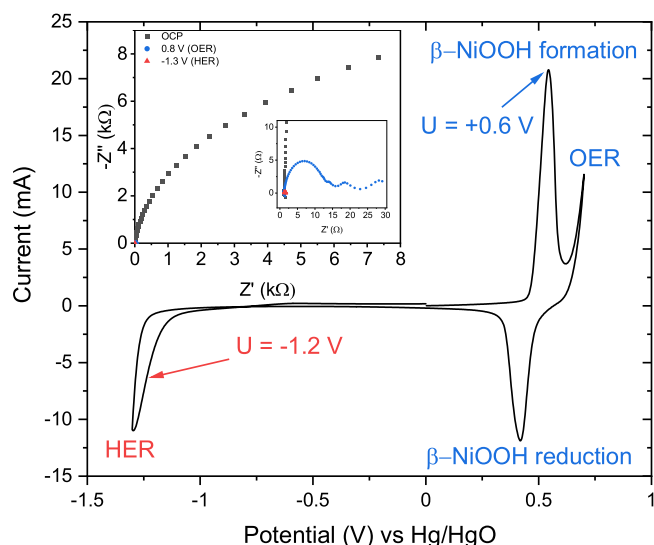


Fig. 2. Electrochemical regions of interest. Cyclic voltammogram of nickel electrode recorded at pH = 14 after performing the experimental procedure and definition of oxidizing and reducing potentials. Two different regions can be distinguished [15,26]: OER and β -NiOOH formation/reduction (blue) and HER (red). The inset on the top left shows the Nyquist plot for Ni under OCP, OER and HER.

X-ray source. Both sources are high flux focused monochromatic X-ray beams that can be scanned across the sample surface to analyze a selected area on the sample surface. The energy scale of the hemispherical analyzer was calibrated according to ISO 15472 by referencing the $Au4f_{7/2}$ and $Cu2p_{3/2}$ main peaks (as measured in situ for corresponding sputter-cleaned, high-purity metal references) to the recommended BE positions of 83.96 eV and 932.62 eV, respectively. The XPS survey spectra, covering a binding energy (BE) range from 0 eV to 1100 eV, were recorded with a step size of 0.25 eV at a constant pass energy of 140 eV using the Al-K α source (power 24.5 W; beam diameter 100 μ m). The XPS detailed regions (i.e., Ni2p, O1s) were extracted from the survey spectra. The HAXPES detailed regions (i.e., Ni2p, O1s) were recorded with a step size of 50 meV at a constant pass energy of 55 eV using the Cr-K α source (51.6 W; beam diameter 91.6 μ m). The

spectra were analyzed using Multipak 9.9 software. Ni2p $_{3/2}$ and O1s regions were fitted using a Gaussian–Lorentzian shape, with a Gaussian contribution of 70%. For metallic core lines, asymmetry of the peak was defined in terms of Tail Length and Tail Scale. A standard Shirley background was used for all the spectra. The atomic concentrations of nickel and oxygen were calculated from the integrated peak areas of the fitted peak components (i.e., Ni2p $_{3/2}$, O1s) using the sensitivity factors provided by the manufacturer (Ulvac-Phi). The fitting of the Ni2p $_{3/2}$ region was performed adapting the results reported from Biesinger et al. [27] for nickel reference samples. The peaks from ‘New line shape for Ni metal’, NiO, Ni(OH) $_2$ and γ -NiOOH with a contribution superior to 5% were employed for fitting and quantification of the several species present in the sample. Some exceptions were made depending on the X-ray source employed for the analysis. Depending on the amount of metallic nickel found in the samples, a different range of binding energy for the Ni2p $_{3/2}$ region was selected. The values of peak separation were fixed either as reported from the author [27] or adapted. For the O1s region, four different contributions of oxygen can be distinguished: oxides (529.6–530.0 eV), hydroxides (531.4–531.7 eV), interstitial water (532.3–532.6 eV) and a last one attributed to surface water and other adsorbed/chemisorbed species arising from the complex electrochemical environment (533.6–533.9 eV) [28–31]. More details can be found in the Supporting Information (Tables T2–T5 and Figs. S2–S33).

From the IMFP values of XPS/HAXPES (see Table T11 in Supporting Information), a probing depth of $3 \cdot \lambda$ can be estimated (3–5 nm for XPS, 15–24 nm for HAXPES). Nevertheless, considering the exponential decay of the signal arising from the different escaping length, an average of 1.5 nm and 6.5 nm can be estimated for XPS and HAXPES, respectively.

The oxide thickness was calculated using the Strohmeier overlayer equation [32] (equation 1 in Supporting Information), making use of the relative intensities arising from the several species. In the case of Ni(OH) $_2$ and NiOOH, hydrated species were used for calculation of the oxide layer thickness, using the density values reported from Bode et al. [13]. Discussion on the results can be found in Section 3.2.

The intensity ratios were converted into elemental concentrations c_i using the calibrated sensitivity factors S_i , including the transmission factor of the instrument by the Multipak software: $c_i = S_i I_i$. The concentration error is estimated to be approximately 5%, considering a

negligible systematic error from S_i and an intensity uncertainty of 5% due to limited signal to noise ratio of better than 100:5.

The concentrations of different chemical species, e.g., Ni-species, were gained from peak analysis. Here, the systematic uncertainty stems from the number and the parameters of the present species assumed, based on chemical intuition and published information, and by qualitative comparison with published spectra. χ^2 of the fits was always smaller than 2.5, which is reasonably good for XPS-peak fitting. This confirms the validity of the assumption; the concentration error of the fitted species (of the applied model) is then solely due to the limited signal to noise ratio as given above; i.e., $\Delta c_i = 5\%$.

2.5. Synchrotron studies

The experiments were conducted at the In Situ Spectroscopy beam-line of Swiss Light Source (SLS), using the Solid-Liquid Interface Chamber (SLIC) endstation [33]. XPS spectra were acquired in a non-baked chamber (base pressure below $5 \cdot 10^{-9}$ mbar), with a linearly polarized light, using a Scienta R4000 HiPP-2 analyzer with an entrance cone aperture diameter of 500 μm and a working distance of 1 mm, operated in a transmission lens mode using a 50 eV pass energy. A first etching treatment was performed on the Ni foil (as described in Section 2.1). After recording the survey and the detail regions (i.e., $\text{Ni}2p_{3/2}$ and $\text{O}1s$), the sample was sputtered for 2 h. The clean sputtered Ni surface was first exposed to 1 mbar H_2O , then to a combination 0.5 mbar H_2O and 0.5 mbar O_2 and in the end to 1 mbar O_2 . Before each exposure step, sample was sputtered again for 2 h to start again from fresh Ni metallic surface. All the spectra were measured with a kinetic energy of 950 eV. Sputtered Au target was used to calibrate the system by adjusting the $\text{Au}4f_{7/2}$ metallic peak to a binding energy of 83.96 eV. Spectra were analyzed using CasaXPS software (version 2.3.24PR1.0) [34]. The $\text{Ni}2p_{3/2}$ and $\text{O}1s$ regions were fitted using a Gaussian (70%) – Lorentzian (30%) shape, defined in CasaXPS as GL(30). For metallic core lines, asymmetry was defined in the form of $\text{LA}(\alpha, \beta, m)$ where α and β define the spread of the tail on either side of the Lorentzian component. The parameter m specifies the width of the Gaussian used to convolute the Lorentzian curve. A standard Shirley background was used for all spectra. The fitting of the $\text{Ni}2p_{3/2}$ region was performed as reported in Section 2.4. For the $\text{O}1s$ region, five different contributions of oxygen can be distinguished: oxides (529.2–529.5 eV), hydroxides (530.5 eV), vapor H_2O (535.3–535.4 eV), gaseous O_2 (538.7 and 539.8 eV) and a last one attributed to adsorbed/chemisorbed species (531.3 eV) [29,30,35,36]. More details can be found in the Supporting Information (Tables T6-T9 and Figs. S34, S35).

2.6. AFM characterization

Atomic force microscopy (AFM) images were measured using a Bruker Dimension Icon 3 atomic force microscope running the 9.7 version of NanoScope software. The images were acquired in Peak Force Tapping mode, using Bruker ScanAsyst-Air cantilevers. Samples were introduced in the system after the electrochemical testing and XPS/HAXPES characterization, with exposure to atmospheric environment. AFM images ($15 \times 15 \mu\text{m}$ and $2 \times 2 \mu\text{m}$) can be found in the Supporting Information (Figs. S39-S44).

2.7. Software

VESTA (version 3) [37] was used for crystal structure visualization, Origin 2022 (version 9.9.0.225) and Igor Pro (version 8.04) for data evaluation, QUASES-IMFP-TTP2M (version 3.0) [38] for calculation of the inelastic mean free path, ImageJ (bundled with 64-bit Java 8) and NanoScope Analysis (version 1.9) for AFM image processing, NOVA (version 2.1.5) for electrochemical data analysis, CasaXPS (version 2.3.24PR1.0) [34] and Multipak (version 9.9) for XPS data analysis.

Table 1

Generic non-electrochemical reactions of Ni with water and oxygen. ΔH 's are based on values of D. G. Archer [44] having a relatively high uncertainty of ± 1 kJ/mol.

| | | |
|--|---------------------------------------|-----|
| $\text{Ni} + \text{H}_2\text{O} \rightleftharpoons \text{NiO} + \text{H}_2$ | $\Delta H = +46 \text{ kJ mol}^{-1}$ | (1) |
| $\text{Ni} + 2\text{H}_2\text{O} \rightleftharpoons \text{Ni}(\text{OH})_2 + \text{H}_2$ | $\Delta H = +42 \text{ kJ mol}^{-1}$ | (2) |
| $\text{Ni} + \frac{1}{2}\text{O}_2 \rightarrow \text{NiO}$ | $\Delta H = -240 \text{ kJ mol}^{-1}$ | (3) |
| $\text{NiO} + \text{H}_2\text{O} \rightarrow \text{Ni}(\text{OH})_2$ | $\Delta H = -4 \text{ kJ mol}^{-1}$ | (4) |

3. Results and discussion

3.1. Initial oxidation of the Ni surface

Even if the preparation of technical electrodes from perfectly clean Ni exposed to controlled UHV environments is unrealistic, the initial state of Ni oxidation by oxygen and water under UHV-compatible conditions has been studied by various authors [39–43]. These studies deliver informations on how a technically pristine surface looks like before electrochemical treatment. Furthermore, a comparison between a surface prepared under UHV-compatible conditions and one prepared under more realistic conditions (glove box with mainly oxygen and water contamination) can be made. So far, all studies known to the authors agree that the reactivity of clean metal surfaces is orders of magnitude less reactive towards H_2O vapor than O_2 gas. The reason for this is the nearly identical heat of formation of water, NiO, and $\text{Ni}(\text{OH})_2$ of -286 kJ/mol , -240 kJ/mol , and 530 kJ/mol , respectively [40,44]. Thus the driving force for oxidation of Ni by water (Eq. (1)) is the entropy change, which in turn is mainly determined by the partial pressure of hydrogen and water ($\Delta S_{\text{reac}} = 58 \text{ J/(mol K)}$). The same is true for the formation of $\text{Ni}(\text{OH})_2$ (Eq. (2)). Intuitively, the direct interaction of O_2 with Ni (Eq. (3)) is more probable, since it is strongly exothermic. The formed NiO may further react with water to form $\text{Ni}(\text{OH})_2$ (Eq. (4)).

Ambient pressure X-ray photoelectron spectroscopy (APXPS) is currently the best approach to bridge the knowledge gap between the metallic pristine surface and the one with native oxide by following the evolution of the Ni- and oxygen species upon exposure to O_2 , H_2O and mixture of O_2 and H_2O up to 1 mbar pressure. The results (Figs. 3 and 4) are in perfect agreement with literature measurements performed at UHV-compatible pressures [39]: at room temperature, water hardly reacts with Ni, showing only gas phase and adsorbed water. In contrast to exposure to O_2 and mixture of both O_2 and H_2O , where the $\text{O}1s$ spectra indicate formation of the oxide and hydroxide in addition to the gas phase species. The intensities of the gas phase signals are slightly smaller than expected from literature data at 1 mbar, likely due to a slight misalignment of the electron analyzer opening. The spectra measured after exposure to the $\text{O}_2/\text{H}_2\text{O}$ mixture resemble the ones obtained post-mortem by ex-situ XPS after dipping in water, showing the formation of $\text{Ni}(\text{OH})_2$. These findings support the thermodynamically favored mechanism, in which Ni is first oxidized by O_2 and subsequently to $\text{Ni}(\text{OH})_2$ by water (reactions (3) and (4)). As the corresponding layers are very thin, trace of oxygen dissolved in water are sufficient to drive reaction (3). The results are relevant, because this surface is the one to be modified once a potential is applied. As UHV-compatible APXPS and post-mortem XPS/HAXPES deliver consistent results, the mechanisms can be traced back to well known atomistic surface science models neglecting the effects from high (ambient) pressures.

3.2. Evolution of the electrode/electrolyte interface

The challenging situation of an electrochemical interface stems from the fact that the outermost surface contains the electro-catalytically active sites, which are defined by the underlying layer, in turn depending on the applied conditions and the sample history. The methods used cover both regions: with an information depth of around 1.5 nm, XPS

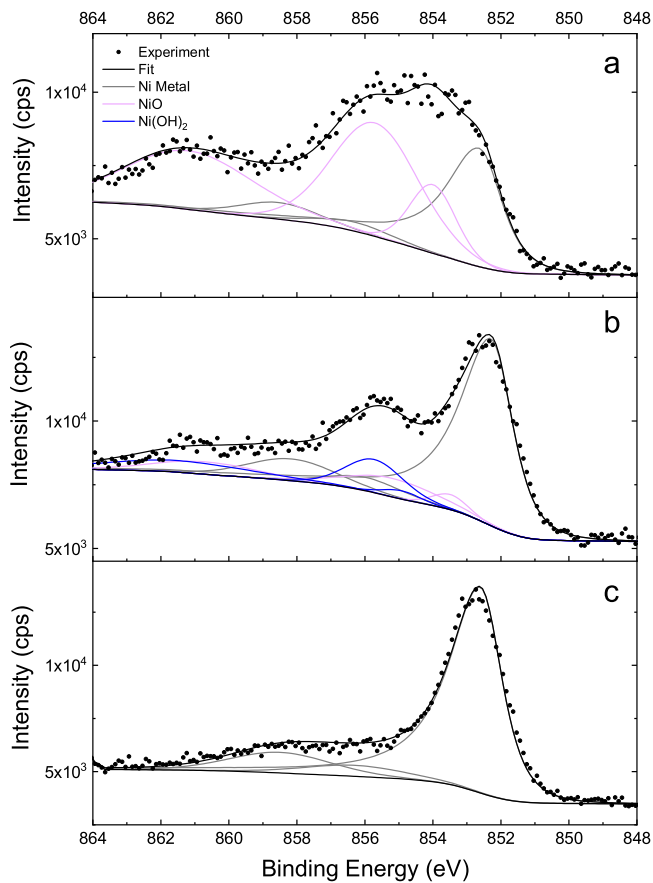


Fig. 3. Evolution of nickel upon gas exposure. APXPS spectra of the Ni2p_{3/2} region after exposure to (a) 1 mbar O₂, (b) 0.5 mbar O₂ + 0.5 mbar H₂O and (c) 1 mbar H₂O. Fittings show how the exposure of Ni surface to the different combinations resulted in the formation of NiO (a) and NiO/Ni(OH)₂ (b), while when exposed just to H₂O (c) no changes are observed from metallic Ni.

is sensitive to the outermost layer, while HAXPES gives the possibility to probe the extended surface up to a depth of 6.5 nm [21,45]. Changes upon gas exposure are commonly referenced to the applied pressure p of the corresponding gas, and then followed as function of time and/or dose, i.e., $\int p(t) dt$. With gas pressures in the mbar range and above, the surface reaches equilibrium quickly; the temporal evolution was too fast to be resolved by the aforementioned photoemission experiments. This is different in electrochemical experiments: the thermodynamic potential change upon applying an electrical potential U is orders of magnitude larger than practically possible by pressure changes ($U \propto \ln p$), and the electrode surface may change over long time periods. The equivalent property of dose in electrochemistry is the accumulated area specific charge C_j/A

$$C_j/A = \int_{t_{j-1}}^{t_j} I(t)/A_j dt \quad (5)$$

with $I(t)$ and A_j the measured current and electrode surface of the run j , respectively. C_j/A is used as effective parameter describing the growth of the (oxy)-hydroxide layer upon electrochemical treatment (Figs. 5, 6, and 7).

Fig. 5 shows the evolution of the relative elemental content of nickel and oxygen as a function of the integrated current upon applying a positive and negative potential. The changes of the elemental concentrations as determined by XPS are relatively small, and hardly change during the course of the experiment. Thus, the outermost surface reaches dynamic equilibrium with the electrolyte on a short time scale (minutes). The changes measured by HAXPES are markedly larger,

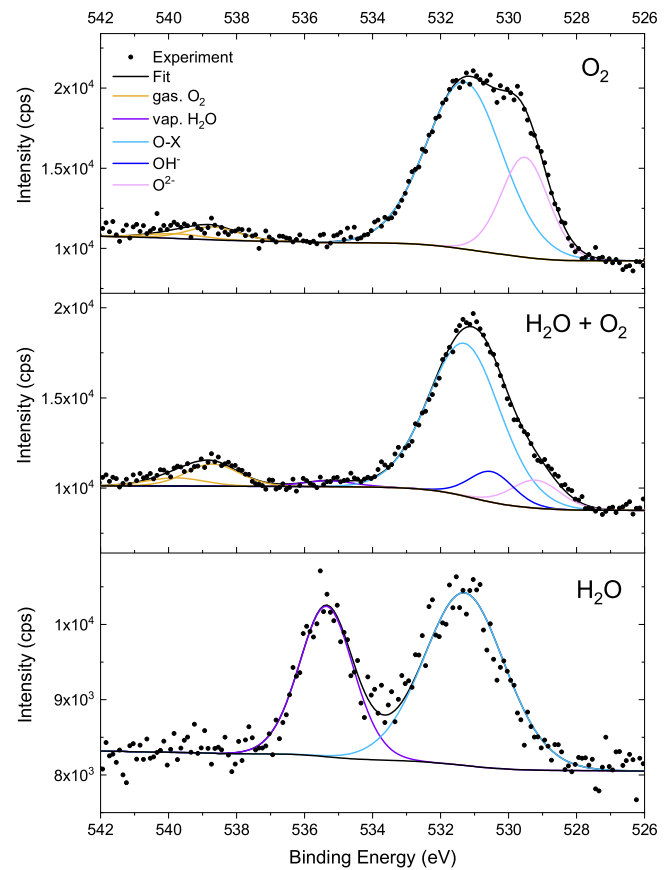


Fig. 4. Evolution of oxygen species upon gas exposure. APXPS spectra of the O1s region after exposure to (a) 1 mbar O₂, (b) 0.5 mbar O₂ + 0.5 mbar H₂O and (c) 1 mbar H₂O. Five different contributions are shown here: oxides (O²⁻), hydroxides (OH⁻), vapor H₂O, gaseous O₂ and adsorbed/chemisorbed species (O-X, with X = H₂, CH₃O₂, ...).

what indicates that the underlying layer thickness continues to grow under oxidizing conditions.

Table T11 and T13 in Supporting Information show the IMFP values calculated considering the different kinetic energies stemming from Ni2p and O1s photoelectron peaks. From those it is possible to observe a more pronounced change in the XPS IMFP values than in the HAXPES ones. When considering then the relative intensities of nickel and oxygen, one should not forget that the two signals are arising from different depths, i.e., nickel intensity will be slightly higher and vice versa slightly lower for the oxygen.

It is worth mentioning at this point the importance of the purification step for the KOH, reported in the section IIB. It has been shown by Trotochaud et al. [7] how Fe impurities can play an important role in enhancing the activity of the Ni-based oxygen evolution reaction (OER) electrocatalyst. The XPS survey (Fig. S45 in Supporting Information) confirms once more the importance of this purification, showing the absence of Fe.

It is tempting to link the thickness d_{n_e} of this layer with the accumulated charge [13,46]:

$$d_{n_e} = \frac{M}{n_e F \rho} C/A \quad (6)$$

Here, M is the molar mass of the layer compound, ρ its density, and n_e is the number of electrons needed to form it. This means that further statements rely on the chemical characterization of the growing layer, which is indeed possible by XPS/HAXPES, and shown in Figs. 6 and 7. However, already a qualitative analysis of the results shows that the chemical structure is too complex to be simplified by a homogeneous

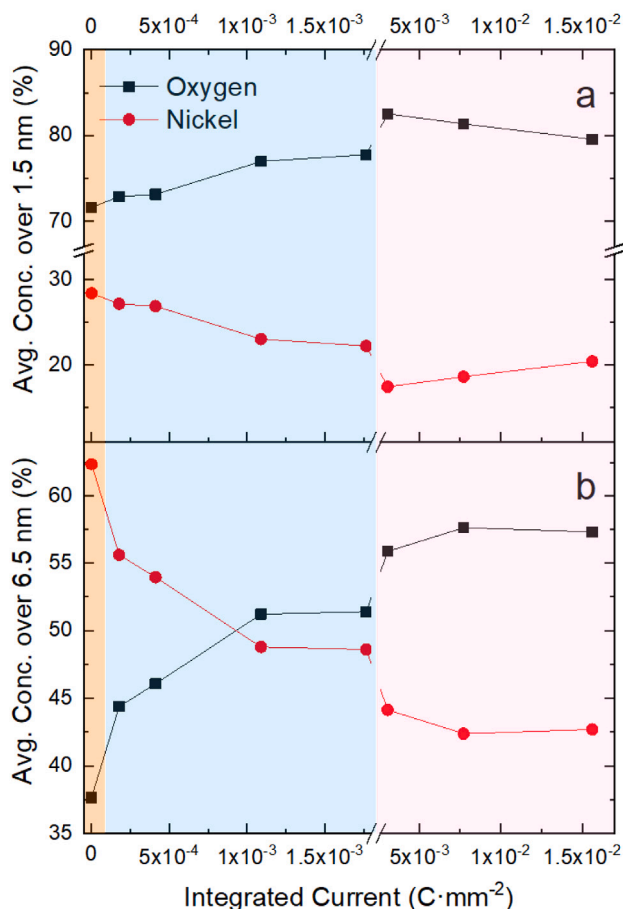


Fig. 5. XPS/HAXPES nickel/oxygen ratio during the process. Evolution of the relative elemental content of nickel and oxygen as a function of the integrated current upon applying a positive and negative potential (polarity change at $1.75 \cdot 10^{-3} \text{ C mm}^{-2}$). Orange, light blue and pink shaded areas indicate OCP, anodic and cathodic conditions, respectively. (a) Top and (b) bottom graphs are derived from XPS (information depth of approx. 1.5 nm), and HAXPES (information depth of approx. 6.5 nm), respectively.

layer with a defined composition. Neglecting this, we can estimate an oxide thickness layer ranging from 0.6 nm to 4.7 nm (see Table T12 in Supporting Information). The oxide layer thickness of XPS and HAXPES calculated from dense bulk densities, do not match exactly. The presence or absence of water in the crystal structure and/or in the pores of the overlayer affects the bulk density and as a consequence the IMFP and thickness too. To account for this, we included a porosity factor of $r_p = 0.35$ multiplied with the densities reported by Bode [13]. The good agreement of XPS and HAXPES with this porosity factor is an additional experimental proof of the porous structure of the overlayer (interstitial water channels, see discussion later).

Before diving into the electrochemical results, we review some details of the potential electrochemical reactions taking place (all reactions are listed in Table 2).

The application of a positive potential triggers the conversion of $\text{Ni}(\text{OH})_2$ to NiOOH (Eq. (7)). The electrochemically assisted growth of NiOOH may also proceed via the formation of NiO (Eq. (9)) and further hydroxylation to NiOOH (Eq. (10)). If one assumes an oxidation reaction ending with NiOOH , the thickness after approximately $1 \cdot 10^{-3} \text{ C mm}^{-2}$ is estimated to be more than 10 nm. However, this value is incompatible with the calculated oxide layer thickness (see Table T12 in Supporting Info).

The situation is comparable to the one during gas absorption. At high doses, the surface saturates quickly, and the sticking coefficient becomes zero. Under electrochemical conditions, the intercalation of

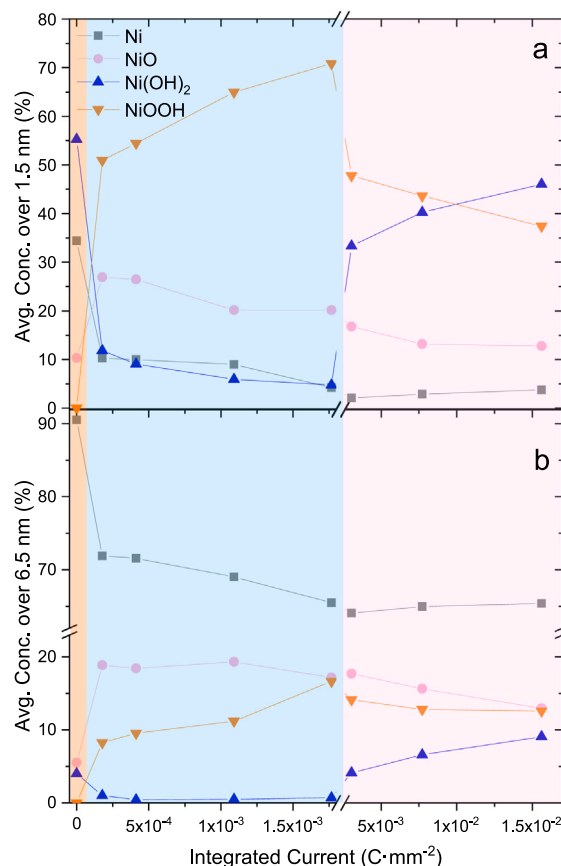


Fig. 6. Nickel modifications during the process. Evolution of the relative amount of Ni compounds as a function of the integrated current upon applying a positive and negative potential (polarity change at $1.75 \cdot 10^{-3} \text{ C mm}^{-2}$). Orange, light blue and pink shaded areas indicate OCP, anodic and cathodic conditions, respectively. (a) Top and (b) bottom graphs are derived from XPS (information depth of approx. 1.5 nm), and HAXPES (information depth of approx. 6.5 nm), respectively.

Table 2

Main electrochemical reactions considered to take place upon applying a potential.

Source: Standard potentials are taken from Ref. [3,15].

| | | |
|---|------------------------------------|------|
| $\text{Ni}(\text{OH})_2 + \text{OH}^- \rightleftharpoons \text{NiOOH} + e^- + \text{H}_2\text{O}$ | $E^0 \approx 0.49 \text{ V (SHE)}$ | (7) |
| $\text{Ni}(\text{OH})_2 \rightleftharpoons \text{NiOOH} + e^- + \text{H}^+$ | $E^0 \approx 0.49 \text{ V (SHE)}$ | (8) |
| $\text{Ni} + 2\text{OH}^- \rightleftharpoons \text{NiO} + \text{H}_2\text{O} + 2e^-$ | $E^0 = 0.11 \text{ V (SHE)}$ | (9) |
| $\text{NiO} + \text{OH}^- \rightleftharpoons \text{NiOOH} + e^-$ | $E^0 \leq 0.49 \text{ V (SHE)}$ | (10) |
| $4\text{OH}^- \rightleftharpoons 2\text{H}_2\text{O} + \text{O}_2 + 4e^-$ | $E^0 = 1.23 \text{ V (SHE)}$ | (11) |
| $2\text{H}_2\text{O} + 2e^- \rightleftharpoons \text{H}_2 + 2\text{OH}^-$ | $E^0 = 0 \text{ V (SHE)}$ | (12) |

oxygen ions into the surface competes with oxygen evolution reaction (Eq. (11)). The majority of the accumulated charge is used to oxidize the hydroxide ions, as the surface is nearly instantaneously oxidized after applying a positive potential (XPS analysis of Ni-species, Fig. 6). The trend is equally reflected by the analysis of the oxygen species (Fig. 7). XPS shows mainly OH^- and interstitial water, with a smaller contribution from O^{2-} and O-X species. The latter can be chemisorbed oxygen, carbon-oxygen species, and surface water. Despite this uncertainty, the relative concentrations change upon polarity switch is in perfect agreement with the electrochemical reactions taking place at the surface. At positive potentials water is formed (Eq. (11)), while it is consumed at negative potentials (Eq. (12)). The ions and water diffusion mechanisms are discussed in more detail later. The behavior is different for the oxygen species as measured by HAXPES. Due to the greater information depth, the oxygen species can be mainly assigned to bulk species.

Although slow, there is a continuing growth of the NiOOH layer under anodic conditions. The evolution of the relative concentration

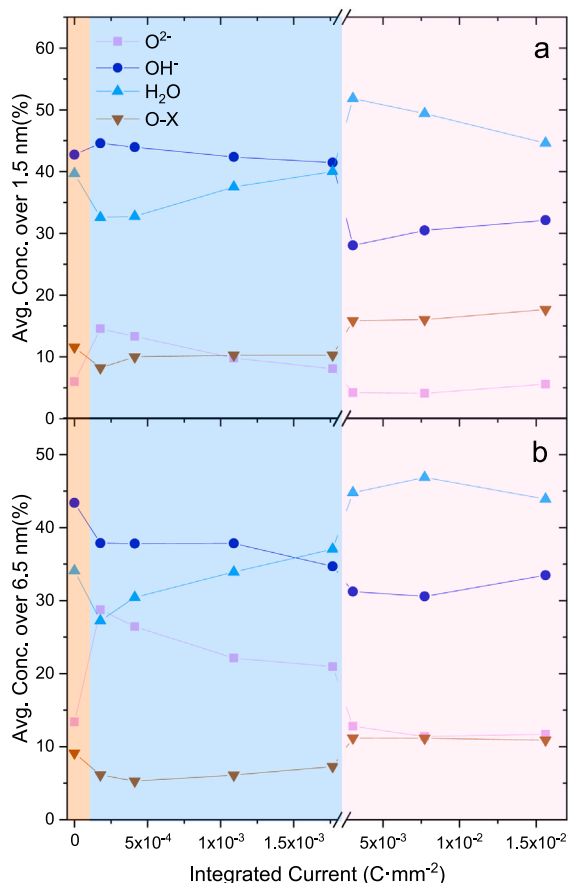
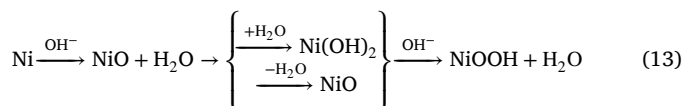


Fig. 7. Oxygen modifications during the process. Evolution of the relative amount of oxygen-compounds as a function of the integrated current upon applying a positive and negative potential (polarity change at $1.75 \cdot 10^{-3} \text{ C mm}^{-2}$). Orange, light blue and pink shaded areas indicate OCP, anodic and cathodic conditions, respectively. (a) Top and (b) bottom graphs are derived from XPS (information depth of approx. 1.5 nm), and HAXPES (information depth of approx. 6.5 nm), respectively. The peak assigned as O²⁻ is indicative of oxygen in NiO and NiOOH, the one assigned as OH⁻ is indicative of hydroxyl in Ni(OH)₂, NiOOH and unspecified hydroxyl groups on the surface, the one assigned as H₂O is indicative of interstitial water and O-X includes adsorbed water and other species on the surface such as C-O-H_x.

for the various species hints at a specific mechanistic pathway (Fig. 6). After the initial formation, the concentrations of NiO and Ni(OH)₂ remain constant, while Ni decreases (Fig. 6). The decrease of the substrate peak indicates the growth of an overlayer on it. The fact that NiO and Ni(OH)₂ remain constant can be explained in two ways: either the phases do not evolve further, and also block any overlayer formation (dead phases), or it acts as intermediate. However, we observe that these phases react upon switching polarity, thus pointing towards the second option, where these intermediates are continuously formed and further react along the reactions described above (Table 2, reactions (9) and (10)):



The presence of Ni(OH)₂ is somewhat surprising, because it is not the most stable compound under positive potentials. However, the oxidation reaction (9) involves the formation of water, which can locally react to form Ni(OH)₂. This is in line with the observation that at high positive potentials and thus high oxidation rate (overcharge) [13,14] corresponding to high local concentration of water, γ -NiOOH is formed, which is basically β -NiOOH with intercalated water [13,47]. At low

rates, water diffusion is comparatively fast and high local water concentrations do not evolve. The important consequence of this mechanism is that fast ion and water diffusion is required to form the anodic overlayer. Vice versa, the formed anodic layer has high mobility for ions and water as is prerequisite for good electro-catalytic activity.

At negative potentials, the process is reversed, i.e., NiOOH converts into Ni(OH)₂ (reversed reaction (7), experimental results in Fig. 6). This process takes place within a few seconds (Figure S36 in Supporting Information), and is thus markedly faster than the formation of NiOOH at positive potentials. After this abrupt change, the system remains stable with only insignificant changes both at the surface (XPS) and in the bulk (HAXPES). Although already known [13,14], these observations demonstrate two important properties of a Ni-electrolyte interface:

- The interface consists always of an (oxy)-hydroxide.
- The (oxy)-hydroxide can easily exchange ions.

Which ions and via which mechanisms depend on the applied potentials and the momentary structure of the surface, and has therefore long been a subject of controversy in the literature. It is important to distinguish the growth of the Ni oxy-hydroxide from the conversion of oxy-hydroxide into the hydroxide: for the latter, only hydrogen diffusion has to be considered and is very fast as observed. For the oxide growth, a bi-directional diffusion is assumed reducing the effective growth rate drastically [48].

3.3. Mechanisms for ions diffusion

The fast conversion of NiOOH to Ni(OH)₂ and vice versa is indication of a high mobility of species in the oxy-hydroxide layer [49,50]. The nature of the mobile species has been debated [14,51]. Simplified, the diffusion species may be electrons, OH⁻ and water following reaction (7), or protons and electrons following Eq. (8). Conceptually, the exchange of OH⁻ and water matches the alkaline environment better than assuming protons. The alternative explanation is that at the electrode-electrolyte interface, protons and hydroxide ions react forming and breaking up water during charging (positive potential) and discharging (negative potential), respectively [50,52]. The proton is then transported through the active material, while the electrons move in the opposite direction. Clear experimental evidence is missing, on one hand due to the complex mechanism, on the other hand due to the complex material and electrochemical environment. Most hints come from electrochemical impedance spectroscopy (EIS) such as shown in Fig. 8 (see also Fig. S37 and S38 in Supporting Information). EIS measurements are considered as the true in situ characterization of the electro-chemical interface, and can be applied at any electro-chemical condition, e.g., at HER and OER potentials (see Fig. 2). However, the measurements take minutes to hours, in which the interface continues to change, if conducted at HER and OER potentials. They make only sense for samples after long-term equilibration (Fig. 2). Furthermore, to link the in situ EIS-results with the consecutive post-mortem XPS/HAXPES characterization, EIS was performed at open-circuit potential to minimize the effect of changes taking place during the EIS procedure.

EIS is sensitive to a variety of phenomena such as the dielectric properties of the evolving oxide layer and the effective hydrogen diffusion in it [15,49,50,53,54] as well as to the electrochemistry taking place at the electrochemical interface. We used a simplified model to simulate the EIS measurements taking into account the electrolyte resistivity and RC-element [55] using a constant phase element (Fig. S46 in Supporting Information), which is a good fit to the frequency range available within the limited time. Additional information such as diffusion needs other potentials than OCP, i.e., at OER and HER, and much prolonged measurement times which are both incompatible with the step-wise procedure we adopted [55]. We thus focus on the first semi-circle revealing properties of both the interface as well as oxide layer. In most cases, the dielectric and conductive properties

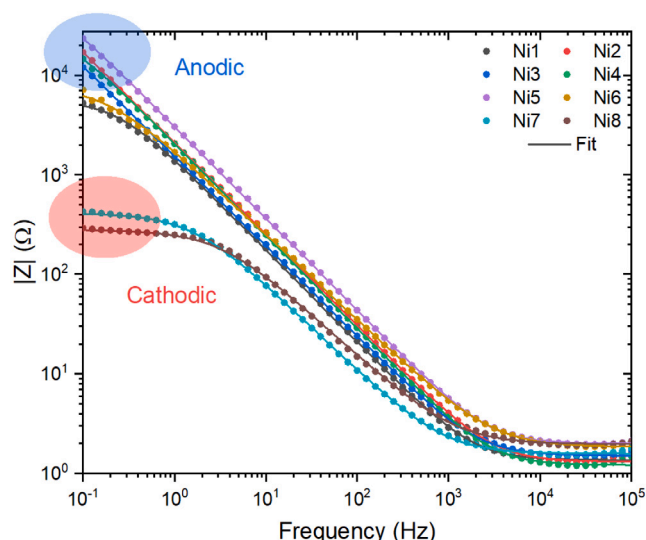


Fig. 8. Electrochemical characterization of the system. Bode plot of the various nickel samples measured in a range between 0.1 to 10^5 Hz, reported as a function of Z . Dots and lines represent experimental results and fittings, respectively. In the graph two different regions are highlighted, referred to the similar trend shown by the samples under anodic (blue) and cathodic (red) conditions. The impedance (Z) of the system decreased from a range of $\sim 10^4$ (anodic) to a range of 10^2 (cathodic) with a factor of ~ 50 . Even though Ni6 is reported as “cathodic” sample, it is not ascribed into the red circle because of its particular properties.

of the electro-chemical double layer are negligible compared to a surface oxide layer [55]. Thus, we assign the changes of the Bode plot shown in Fig. 8 to the oxide layer (see Table T15 and Fig. S46 in Supporting Information). In particular, we observe a marked increase of the conductivity upon change of polarity. The first spectrum at reducing conditions after long term oxidation (sample Ni6 in Fig. 8, compare also Figs. S36, S37, S38, and S46 in Supporting Information) is particularly interesting. It still shows the characteristics of the oxide layer at oxidizing conditions, i.e., the modifications at reducing potential were not yet sufficient to change all of the NiOOH to Ni(OH)₂ (compare also Fig. 7).

The change of conductivity from NiOOH to Ni(OH)₂ is in disagreement with Ref. [53], if considering only dry (oxy)-hydroxides, where opposite behavior was observed. However, Motori et al. reported an extreme dependence of the conductivity on the water content in the coating. With this, the enhanced conductivity of oxide layer under reducing condition is in perfect line with our observations from XPS/HAXPES, when a clear increase in the water content during the cathodic process is observed (Fig. 7), highlighting once more the importance of interstitial water. Indeed, both reactions, Eqs. (10) and (8) relying on H⁺ and OH⁻ diffusion, respectively, require a high electronic conductivity. Under consideration of the charge neutrality, a diffusion coefficient of the counter ion can be derived, but not its chemical state (i.e., H⁺ or OH⁻). More fundamental methods to study the hydrogen dynamics such as neutron scattering [56] are needed, but are difficult to employ as operando methods [47]. Without such independent methods, the nature of the diffusing species remains elusive [14].

Wehrens-Dijksma and Notten give a hint how to elucidate the mechanism [14]: the main difference between Eqs. (10) and (8) is that for OH⁻ diffusion, water has to diffuse in the opposite direction [57]. Furthermore, additional cations such as potassium K⁺ may be involved. The HAXPES measurements are ideal to verify the corresponding hypothesis. We do not find any potassium at any state of experiment, excluding any cations involved in the diffusion mechanism. Furthermore, we find an increase of the relative intensity of the peak assigned to interstitial water in the course of the experiment (Fig. 7). The measurements thus show that water accumulates both in the NiOOH and Ni(OH)₂ layer, i.e., during oxidation and reduction, respectively;

which is strong evidence for the OH⁻ diffusion mechanism (reaction (10)) as proposed by Mo et al. [57].

Water and OH⁻ ion mobility in the bulk is very slow; thus Yoon and Pyun [54] favor proton and electron transport (reaction (8)), with the conversion of OH⁻ to proton and electrons taking place at the surface. However, even proton diffusion is very slow; thus Briggs and Fleischmann [58] suggested diffusion along the internal surfaces of crystallites already in 1971. This suggestion is experimentally confirmed by our findings, in particular by the observation of water accumulation in the bulk as shown in Fig. 7. This means that an overlayer grown electrochemically has the optimal nano-structure of an electrode. Various nano-structures can be formed by anodization [59]. Only growing overlayers at the conditions where it is supposed to be used as electrode leads to the right electro-catalytic properties. The NiOOH layer has a low conductivity (Fig. 8), its growth during positive potentials is self-hindering with thickness (Fig. S36 in Supporting Information). Changing to negative potentials converts the layer into highly conductive layer consisting mainly of Ni(OH)₂ (Fig. 8). Dry Ni(OH)₂ is an insulator [53] with a lower conductivity than NiOOH. However, the conductivity of electro-chemically generated Ni(OH)₂ increases drastically by eight orders of magnitude from dry to wet Ni(OH)₂ with 2 weight% water absorbed [53]. The reduction from NiOOH to Ni(OH)₂ goes along with incorporation of water, as observed by the observed increase of the water content in the layer (Fig. 5), and as underlined by simple consideration of the reaction mechanism (reaction scheme (13)). With the higher conductivity, water can be transported much more easily, being the precursors of the channels for ion transport, once back to positive potentials. As the conversion of OH⁻ to proton and electrons can take place only at the surface, a high surface area is crucial. Interestingly, the intercalation of hydrogen into NiOOH has an additional effect: the cell volume increases by 18% [25,60], which is translated into a large compressive stress, released by pushing some material outward in the form of ridges. We applied atomic force microscopy (AFM) to probe the surface structure of the electrodes (Fig. 9). As the measurements were conducted ex-situ, further changes by the exposure to air cannot be excluded. We thus limit the discussion on qualitative changes between the pristine and treated samples. The macroscopic morphology is dominated by relatively large grains of the polycrystalline materials of around 400 nm. On the nanometer scale, the surface is relatively smooth before and after application of oxidizing conditions, showing only small and gentle ridges and nano-scale grains, indication of a closed passivation layer. Here, growth can take place only via transport of ions through the bulk, which is very slow [48], and thus stops at relatively small layer thickness. After applying a negative potential, the AFM images show the appearance of ridges. The cracking and formation of these ridges facilitate ion diffusion and thus oxide growth, and increase the surface area. The observed water content explains the high conductivity of the electro-chemically formed Ni(OH)₂, which has negligible conductivity in the water-free phase [53].

This explains the exceptional properties of self-organized Ni (oxy)-hydroxide layer, and why specific electrochemical cycling improves electro-catalysis [4]. Conversely, an improvement by an intelligent design of an optimized nanostructure is challenging. E.g., Gabler et al. [61] demonstrated the increase of the surface area of electrodes by pulsed laser-structuring; however, the activity was mainly determined by the subsequently applied electrochemical treatment. The self-organization also enables the self-healing of electrodes as recently found by Thorarinsdottir et al. [62].

This study does not give concrete recipes to improve electro-catalytic activity. However, it is obvious that the electrochemical conditions including chemistry, i.e., host metal/alloy, impurity ions such as iron [7], pH, applied fields (electrical potential, magnetic fields [63]), and process parameters (time, cycling) will affect the performance of the electrode. Fig. 9 gives an illustrative summary of the structure of the Ni oxy-hydroxide layers. We would like to highlight that knowledge

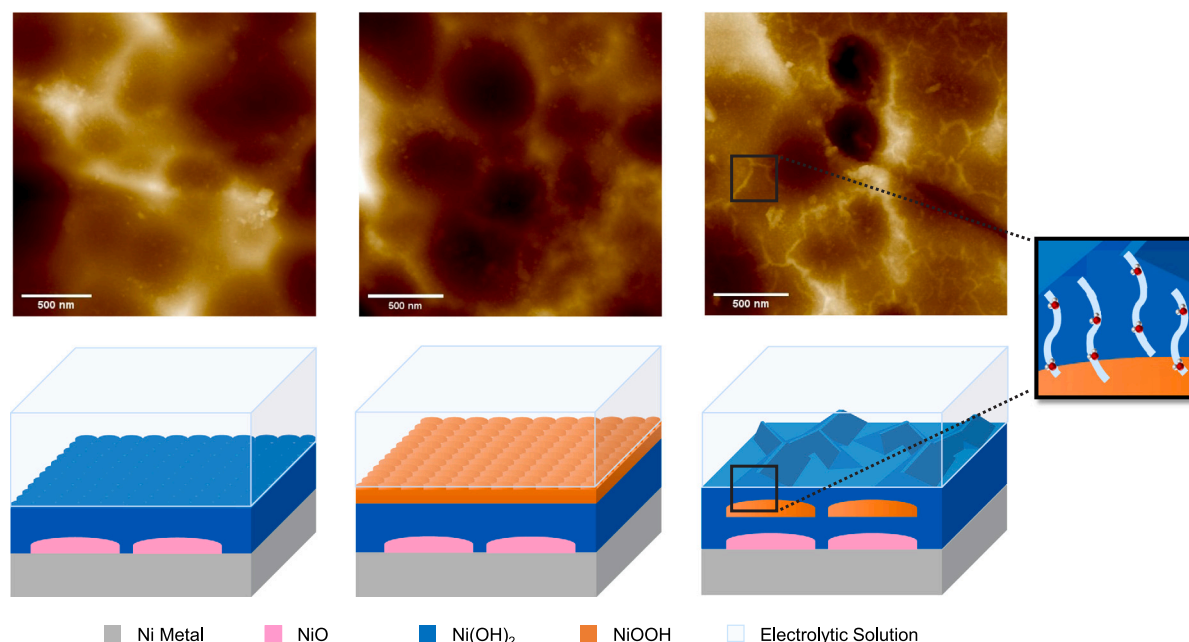


Fig. 9. Model of the electrode/electrolyte interface after subsequent electrochemical treatments. AFM images (top) and corresponding model (bottom) showing the formation of a first layer of NiO and Ni(OH)₂ after exposure to the electrolytic solution under OCP (left), formation of a NiOOH layer under anodic conditions (center) and formation of Ni(OH)₂ under cathodic conditions (right). The scale bar on the AFM images is 500 nm, and colormap shows the min. to max. height information (dark to light). For each case considered the max. height is 150, 125 and 178 nm, respectively. The enlargement from cathodic conditions shows the creation of ridges due to lattice expansion, where channels are spread all over the passivation layer, allowing the transport of water and ions from the surface to the bulk and vice versa.

of the elementary reaction mechanism at the electrode–electrolyte interface alone is not sufficient to characterize the performance of an electrode. The study and optimization of such interfaces requires analysis methods such as demonstrated in this paper, being able to probe deeper than the active electrode–electrolyte interface.

4. Conclusions

In this work, we report a full picture of the changes occurring on the Ni surface exposed to harsh conditions during the water splitting process. In addition to established characterization techniques, we applied a combination of in situ impedance spectroscopy with post-mortem XPS/HAXPES. In particular, the comparison of the distribution of Ni (oxy)-hydroxides, as well as water formed during the electrochemical process at different depths as made possible by XPS and HAXPES, allows conclusions on the corresponding electrochemical mechanisms. The observations explain in an elegant way the occurrence of the water containing allotropes during electro-catalysis. Growth of the anodic layer requires a high mobility of ions and water, being a by-product of the reaction. The material produced in this way must therefore have a high mobility of water and OH[−] ions. Interestingly, the bulk mobility is relatively low. This means that the OH[−] ions diffusion is unlikely to take place in the bulk over long distances. Thus, the growth mechanism of the oxy-hydroxide layers is the key to the peculiar structure which enables high electrocatalytic activity by high surface area and short diffusion pathways. While we do not study the self-organization of the structure in detail, the findings explain why intelligent design of electrode nano-structure by external treatment has led to moderate progress only.

In addition to the specific findings, our work demonstrates the feasibility of a new way to investigate the evolution of layers at the electrode–electrolyte interface under relevant catalytic conditions. Furthermore, it paves the way for the investigation of more complex systems (e.g., alloys, nanostructured materials, multilayered systems...) with applications in different fields such as catalysis, optoelectronic devices, batteries, just to cite some.

CRediT authorship contribution statement

Filippo Longo: Conception of experiments, Experimental work, Data evaluation, Writing of manuscript. **Emanuel Billeter:** Experimental work (beam time), Data evaluation. **Selim Kazaz:** Experimental work (beam time), Data evaluation. **Alessia Cesarini:** Experimental work (beam time), Data evaluation. **Marin Nikolic:** Experimental work (beam time), Data evaluation. **Aarati Chacko:** Experimental work (AFM), Data evaluation. **Patrik Schmutz:** Experimental support. **Zbynek Novotny:** Experimental work (APXPS), Data evaluation. **Andreas Borgschulte:** Conception of experiments, Experimental work, Data evaluation, Writing of manuscript.

Declaration of competing interest

The authors declare that they have no known competing financial interests or personal relationships that could have appeared to influence the work reported in this paper.

Data availability

The data that support the findings of this study are available under <https://doi.org/10.5281/zenodo.8376729>.

Acknowledgments

We thank Dr. Roland Hauert and Dr. Lars P. H. Jeurgens for the fruitful discussion. This work is supported by LightChEC and by the SNF grant n° 182987. Part of this work was performed at the In Situ Spectroscopy (X07DB) beamline of the Swiss Light Source, Paul Scherrer Institut, Villigen PSI, Switzerland. All authors have given approval to the final version of the manuscript.

Appendix A. Supplementary data

Supplementary material related to this article can be found online at <https://doi.org/10.1016/j.susc.2023.122397>.

References

- [1] A. Mavri, C. Cui, Advances and challenges in industrial-scale water oxidation on layered double hydroxides, *ACS Appl. Energy Mater.* 4 (11) (2021) 12032–12055.
- [2] D.M.F. Santos, C.A.C. Sequeira, *Quim. Nova* 36 (2013) 1176–1193.
- [3] M. Pourbaix, *Atlas of Electrochemical Equilibria in Aqueous Solutions*, National Association of Corrosion Engineers, 1974.
- [4] S.L. Medway, C.A. Lucas, A. Kowal, R.J. Nichols, D. Johnson, *J. Electroanal. Soc.* 587 (1) (2006) 172–181.
- [5] L.-F. Huang, M.J. Hutchison, R.J. Santucci Jr., J.R. Scully, J.M. Rondinelli, *J. Phys. Chem. C* 121 (18) (2017) 9782–9789.
- [6] L.J. Enman, M.S. Burke, A.S. Batchellor, S.W. Boettcher, Effects of intentionally incorporated metal cations on the oxygen evolution electrocatalytic activity of nickel (oxy)hydroxide in alkaline media, *ACS Catal.* 6 (4) (2016) 2416–2423.
- [7] L. Trotochaud, S.L. Young, J.K. Ranney, S.W. Boettcher, Nickel–Iron oxyhydroxide oxygen-evolution electrocatalysts: The role of intentional and incidental iron incorporation, *J. Am. Chem. Soc.* 136 (18) (2014) 6744–6753.
- [8] J. Zhang, J.R. Winkler, H.B. Gray, B.M. Hunter, Mechanism of Nickel–Iron water oxidation electrocatalysts, *Energy Fuels* 35 (23) (2021) 19164–19169.
- [9] Z. Yu, Y. Bai, G. Tsekouras, Z. Cheng, Recent advances in Ni-Fe (Oxy)hydroxide electrocatalysts for the oxygen evolution reaction in alkaline electrolyte targeting industrial applications, *Nano Select* 3 (4) (2022) 766–791.
- [10] H. Ali-Löytty, M.W. Louie, M.R. Singh, L. Li, H.G. Sanchez Casalongue, H. Ogasawara, E.J. Crumlin, Z. Liu, A.T. Bell, A. Nilsson, D. Friebel, Ambient-pressure XPS study of a Ni-Fe electrocatalyst for the oxygen evolution reaction, *J. Phys. Chem. C* 120 (4) (2016) 2247–2253.
- [11] M.S. Burke, S. Zou, L.J. Enman, J.E. Kellon, C.A. Gabor, E. Pledger, S.W. Boettcher, Revised oxygen evolution reaction activity trends for first-row transition-metal (oxy)hydroxides in alkaline media, *J. Phys. Chem. Lett.* 6 (18) (2015) 3737–3742.
- [12] M.W. Louie, A.T. Bell, An investigation of thin-film Ni-Fe oxide catalysts for the electrochemical evolution of oxygen, *J. Am. Chem. Soc.* 135 (33) (2013) 12329–12337.
- [13] H. Bode, K. Dehmelt, J. Witte, Zur kenntnis der nickelhydroxidelektrode. II. über die oxydationsprodukte von nickel(II)-hydroxiden, *Z. Anorg. Allg. Chem.* 366 (1–2) (1969) 1–21.
- [14] M. Wehrens-Dijkstra, P. Notten, Electrochemical quartz microbalance characterization of Ni(OH)₂-based thin film electrodes, *Electrochim. Acta* 51 (18) (2006) 3609–3621.
- [15] M. Alsabet, M. Grdeń, G. Jerkiewicz, Electrochemical growth of surface oxides on nickel. Part 3: Formation of β -NiOOH in relation to the polarization potential, polarization time, and temperature, *Electrocatalysis* 6 (2015) 60–71.
- [16] G. Righi, J. Plescher, F. Schmidt, On the origin of multihole oxygen evolution in haematite photoanodes, *Nat. Catal.* 5 (2022) 888–899.
- [17] S. Corby, M.-G. Tecedor, S. Tengeler, C. Steinert, B. Moss, C.A. Mesa, H.F. Heiba, A.A. Wilson, B. Kaiser, W. Jaegermann, L. Francàs, S. Gimenez, J.R. Durrant, Separating bulk and surface processes in NiOx electrocatalysts for water oxidation, *Sustain. Energy Fuels* 4 (2020) 5024–5030.
- [18] F.A. Stevie, C.L. Donley, Introduction to x-ray photoelectron spectroscopy, *J. Vacuum Sci. Technol. A* 38 (6) (2020) 063204.
- [19] D. Ketencioğlu, A general overview and comparative interpretation on element-specific X-ray spectroscopy techniques: XPS, XAS, and XRS, *X-Ray Spectr.* 1 (2022) 422–443.
- [20] C. Kalha, et al., Hard x-ray photoelectron spectroscopy: a snapshot of the state-of-the-art in 2020, *J. Phys.: Condens. Matter* 33 (23) (2021) 233001.
- [21] O. Sambalova, E. Billeter, J. Mann, T. Miyayama, D. Burnat, A. Heel, D. Bleiner, A. Borgschulte, Hard and soft X-ray photoelectron spectroscopy for selective probing of surface and bulk chemical compositions in a perovskite-type Ni catalyst, *Surf. Interface Anal.* 52 (12) (2020) 811–817.
- [22] M. Grdeń, M. Alsabet, G. Jerkiewicz, Surface science and electrochemical analysis of nickel foams, *ACS Appl. Mater. Interfaces* 4 (6) (2012) 3012–3021.
- [23] T.E. Graedel, C.J. Leygraf, Corrosion mechanisms for nickel exposed to the atmosphere, *Electrochim. Soc.* 147 (3) (2000) 1010–1014.
- [24] L.M.M. de Souza, F.P. Kong, F.R. McLarnon, R.H. Muller, Spectroscopic ellipsometry study of nickel oxidation in alkaline solution, *Electrochim. Acta* 42 (8) (1997) 1253–1267.
- [25] M. Casas-Cabanas, M.D. Radin, J. Kim, C.P. Grey, A. Van der Ven, M.R. Palacín, The nickel battery positive electrode revisited: stability and structure of the β -NiOOH phase, *J. Mater. Chem. A* 6 (2018) 19256–19265.
- [26] K. Juodkazis, J. Juodkazytė, R. Vilkauskaitė, V. Jasulaitienė, Nickel surface anodic oxidation and electrocatalysis of oxygen evolution, *J. Solid State Electrochem.* 12 (11) (2008) 1469–1479.
- [27] M.C. Biesinger, B.P. Payne, L.W.M. Lau, A. Gerson, R.S.C. Smart, X-ray photoelectron spectroscopic chemical state quantification of mixed nickel metal, oxide and hydroxide systems, *Surf. Interface Anal.* 41 (4) (2009) 324–332.
- [28] J. Linn, W. Swartz, An XPS study of the water adsorption/desorption characteristics of transition metal oxide surfaces: Microelectronic implications, *Appl. Surf. Sci.* 20 (1) (1984) 154–166.
- [29] M.C. Biesinger, B.P. Payne, A.P. Grosvenor, L.W. Lau, A.R. Gerson, R.S. Smart, Resolving surface chemical states in XPS analysis of first row transition metals, oxides and hydroxides: Cr, Mn, Fe, Co and Ni, *Appl. Surf. Sci.* 257 (7) (2011) 2717–2730.
- [30] B. Payne, M. Biesinger, N. McIntyre, Use of oxygen/nickel ratios in the XPS characterisation of oxide phases on nickel metal and nickel alloy surfaces, *J. Electron Spectrosc. Relat. Phenom.* 185 (5) (2012) 159–166.
- [31] M. Fingerle, S. Tengeler, W. Calvet, T. Mayer, W. Jaegermann, Water interaction with sputter-deposited nickel oxide on n-Si photoanode: Cryo photoelectron spectroscopy on adsorbed water in the frozen electrolyte approach, *J. Electrochem. Soc.* 165 (4) (2018) H3148.
- [32] B.R. Strohmeier, An ESCA method for determining the oxide thickness on aluminum alloys, *Surf. Interface Anal.* 15 (1) (1990) 51–56.
- [33] Z. Novotny, D. Aegerter, N. Comini, B. Tobler, L. Artiglia, U. Maier, T. Moehl, E. Fabbri, T. Huthwelker, T.J. Schmidt, M. Ammann, J.A. van Bokhoven, J. Raabe, J. Osterwalder, Probing the solid–liquid interface with tender x rays: A new ambient-pressure x-ray photoelectron spectroscopy endstation at the swiss light source, *Rev. Sci. Instrum.* 91 (2) (2020) 023103.
- [34] N. Fairley, V. Fernandez, M. Richard-Plouet, C. Guillot-Deudon, J. Walton, E. Smith, D. Flahaut, M. Greiner, M. Biesinger, S. Tougaard, D. Morgan, J. Baltrusaitis, Systematic and collaborative approach to problem solving using X-ray photoelectron spectroscopy, *Appl. Surf. Sci. Adv.* 5 (2021) 100112.
- [35] S. Yamamoto, T. Kendelewicz, J.T. Newberg, G. Ketteler, D.E. Starr, E.R. Mysak, K.J. Andersson, H. Ogasawara, H. Bluhm, M. Salmeron, G.E. Brown, A. Nilsson, Water adsorption on α -Fe₂O₃(0001) at near ambient conditions, *J. Phys. Chem. C* 114 (5) (2010) 2256–2266.
- [36] T.G. Avval, S. Chatterjee, G.T. Hodges, S. Bahr, P. Dietrich, M. Meyer, A. Thiß en, M.R. Linford, Oxygen gas, O₂(g), by near-ambient pressure XPS, *Surf. Sci. Spectra* 26 (1) (2019) 014021.
- [37] K. Momma, F. Izumi, VESTA 3 for three-dimensional visualization of crystal, volumetric and morphology data, *J. Appl. Crystallogr.* 44 (2011) 1272–1276.
- [38] S. Tanuma, C.J. Powell, D.R. Penn, Calculations of electron inelastic mean free paths. V. Data for 14 organic compounds over the 50–2000 eV range, *Surf. Interfaces Anal.* 21 (1994) 165.
- [39] B. Payne, M. Biesinger, N. McIntyre, The study of polycrystalline nickel metal oxidation by water vapour, *J. Electron Spectrosc. Relat. Phenom.* 175 (1) (2009) 55–65.
- [40] C. Benndorf, C. Nöbl, M. Rusenberg, F. Thieme, H₂O interaction with clean and oxygen precovered Ni(110), *Surf. Sci.* 111 (1) (1981) 87–101.
- [41] C. Benndorf, C. Nöbl, F. Thieme, Interaction of H₂O with a clean and oxygen precovered Ni(110) surface studied by XPS, *Surf. Sci.* 121 (2) (1982) 249–259.
- [42] J. Heras, E. Albano, Interaction of water molecules with polycrystalline films of Fe, Co and Ni with different surface roughness: II. Water adsorption on water pretreated and passivated films, *Appl. Surf. Sci.* 17 (2) (1983) 220–230.
- [43] A. Carley, S. Rassias, M. Roberts, The specificity of surface oxygen in the activation of adsorbed water at metal surfaces, *Surf. Sci.* 135 (1) (1983) 35–51.
- [44] D.G. Archer, Thermodynamic properties of import to environmental processes and remediation. II. Previous thermodynamic property values for nickel and some of its compounds, *J. Phys. Chem. Ref. Data* 28 (5) (1999) 1485.
- [45] S. Siol, J. Mann, J. Newman, T. Miyayama, K. Watanabe, P. Schmutz, C. Cancellieri, L.P. Jeurgens, Concepts for chemical state analysis at constant probing depth by lab-based XPS/HAXPES combining soft and hard X-ray sources, *Surf. Interface Anal.* 52 (12) (2020) 802–810.
- [46] G. Briggs, P. Snodin, Ageing and the diffusion process at the nickel hydroxide electrode, *Electrochim. Acta* 27 (5) (1982) 565–572.
- [47] D.S. Hall, D.J. Lockwood, C. Bock, B.R. MacDougall, Nickel hydroxides and related materials: a review of their structures, synthesis and properties, *Proc. R. Soc. Lond. Ser. A Math. Phys. Eng. Sci.* 471 (2174) (2015) 20140792.
- [48] S. Mrowec, Z. Grzesik, Oxidation of nickel and transport properties of nickel oxide, *J. Phys. Chem. Solids* 65 (10) (2004) 1651–1657.
- [49] H. Ewe, Oberflächendiffusion auf oxidiertem nickel, *Electrochim. Acta* 18 (2) (1973) 127–132.
- [50] S. Motupally, C.C. Streinz, J.W. Weidner, Proton diffusion in nickel hydroxide films: Measurement of the diffusion coefficient as a function of state of charge, *J. Electrochem. Soc.* 142 (5) (1995) 1401–1408.
- [51] J. Zaffran, M.B. Stevens, C.D.M. Trang, M. Nagli, M. Shehadeh, S.W. Boettcher, M. Caspari Toroker, Influence of electrolyte cations on Ni(Fe)OOH catalyzed oxygen evolution reaction, *Chem. Mater.* 29 (11) (2017) 4761–4767.
- [52] M. Ortiz, D. Becker, G. Garaventa, A. Visintin, E. Castro, S. Real, Dynamic monitoring of structural changes in nickel hydroxide electrodes during discharge in batteries, *Electrochim. Acta* 56 (23) (2011) 7946–7954.
- [53] A. Motori, F. Sandrolini, G. Davolio, Electrical properties of nickel hydroxide for alkaline cell systems, *J. Power Sources* 48 (3) (1994) 361–370.
- [54] Y.-G. Yoon, S.-I. Pyun, Hydrogen transport through nickel hydroxide film: current transient analysis, *Electrochim. Acta* 42 (16) (1997) 2465–2474.
- [55] A.R.C. Bredar, A.L. Chown, A.R. Burton, B.H. Farnum, Electrochemical impedance spectroscopy of metal oxide electrodes for energy applications, *ACS Appl. Energy Mater.* 3 (1) (2020) 66–98.
- [56] R. Baddour-Hadjean, F. Fillaux, J. Tomkinson, Proton dynamics in β -Ni(OH)₂ and β -NiOOH, *Physica B* 213–214 (1995) 637–639.

- [57] Y. Mo, E. Hwang, D.A. Scherson, In situ quartz crystal microbalance studies of nickel hydrous oxide films in alkaline electrolytes, *J. Electrochem. Soc.* 143 (1) (1996) 37–43.
- [58] G.W.D. Briggs, M. Fleischmann, Oxidation and reduction of nickel hydroxide at constant potential, *Trans. Faraday Soc.* 67 (1971) 2397–2407.
- [59] H. Chik, J. Xu, Nanometric superlattices: non-lithographic fabrication, materials, and prospects, *Mater. Sci. Eng. R* 43 (4) (2004) 103–138.
- [60] V. Kazimirov, M. Smirnov, L. Bourgeois, L. Guerlou-Demourgues, L. Servant, A. Balagurov, I. Natkaniec, N. Khasanova, E. Antipov, Atomic structure and lattice dynamics of Ni and Mg hydroxides, *Solid State Ion.* 181 (39) (2010) 1764–1770.
- [61] A. Gabler, C.I. Müller, T. Rauscher, M. Köhring, B. Kieback, L. Röntzsch, W. Schade, Ultrashort pulse laser-structured nickel surfaces as hydrogen evolution electrodes for alkaline water electrolysis, *Int. J. Hydrogen Energy* 42 (16) (2017) 10826–10833.
- [62] A. Thorarinsdottir, S. Veroneau, D. Nocera, Self-healing oxygen evolution catalysts, *Nature Commun.* 13 (2022) 1243.
- [63] O. Sambalova, E. Billeter, O. Yildirim, A. Sterzi, D. Bleiner, A. Borgschulte, Magnetic field enhancement of electrochemical hydrogen evolution reaction probed by magneto-optics, *Int. J. Hydrogen Energy* 46 (5) (2021) 3346–3353.